Experimental Validation of a Gamma Detector With a Novel Light-Guide-PMT Geometry to Reduce Dead Edge Effects

Wang, Beien; Kreuger, Rob; Huizenga, Jan; Beekman, Freek J.; Goorden, Marlies C.

DOI
10.1109/TRPMS.2019.2916386

Publication date
2020

Document Version
Final published version

Published in
IEEE Transactions on Radiation and Plasma Medical Sciences

Experimental Validation of a Gamma Detector With a Novel Light-Guide-PMT Geometry to Reduce Dead Edge Effects

Beien Wang, Rob Kreuger, Jan Huizenga, Freek J. Beekman, and Marlies C. Goorden

***Abstract*—Photomultiplier tube (PMT)-based scintillation cameras are predominant in molecular imaging but have the drawback that position estimation is severely degraded near the edges (dead edge effect). This leads to sensitivity losses and can cause severe problems in applications like molecular breast imaging and in certain SPECT devices. Using smaller light sensors or semiconductor detectors can solve this issue but leads to increased costs. Here we present a gamma detector based on standard PMTs with a novel light-guide-PMT geometry that strongly reduces dead edges. In our design, a monolithic NaI(Tl) scintillator is read out by square PMTs placed in a staggered arrangement. At the edge of the scintillator we inserted additional light-guides to emulate half-size PMTs. Detector performance was assessed for ^{99m}Tc imaging; an average spatial resolution of 3.6 mm was measured over the whole detector, degrading to 4.0 mm within 30 mm to the critical edge. The dead edge of the scintillator is <3 mm. Since a 12-mm seal was used, the overall dead edge is <15 mm, which is a significant improvement over conventional Anger cameras (∼40-mm dead edge). Therefore, the presented geometry can be useful in creating economical gamma detectors with reduced dead edges.**

***Index Terms*—Anger camera, dead edge, gamma detector, light-guide, molecular breast imaging, scintillator.**

I. Introduction

GAMMA detectors used in nuclear medicine are mostly based on NaI(Tl) scintillators read out by an array of photomultiplier tubes (PMTs) that estimate the gamma interaction positions using Anger logic [1]. These gamma detectors, often referred to as Anger cameras, give satisfactory position and energy resolution, have good detection efficiency, and are relatively cost-effective. However, Anger cameras also have the drawback of poor spatial linearity and resolution at the scintillator's edges, which is often referred to as the dead edge effect [2]–[4]. Although not being able to use the whole scintillator surface always has the drawback of sensitivity loss, it is accepted in most clinical whole-body SPECT scanners in which the rotating Anger cameras are large and not using the edges of the cameras does not automatically lead to artefacts. In contrast, in some applications, dead edges as large as in conventional Anger cameras (roughly 4 cm which corresponds to the radius of the PMTs) are completely unacceptable. For example, in some dedicated cardiac SPECT systems, multiple relatively small stationary gamma camera modules are closely surrounding the chest in order to increase count yield from the heart on which they focus [5], [6], and large dead edges will result in large gaps between active detector areas and thus compromised sampling completeness. Additionally, in molecular breast imaging, in which the detectors are put close to the chest wall [7], [8], the use of conventional Anger cameras will result in being unable to image breast tissue near the chest.

To improve spatial resolution and linearity near the edges, current solutions mostly involve using small light sensors (e.g., position-sensitive PMTs and silicon photomultipliers) and/or scintillator pixelization [6], [9]–[20]. Semiconductor gamma detectors which convert gamma energy directly into electric signal are also an option to reduce dead edges and these have already been applied in some applications [5], [21]–[25]. However, all these solutions come at a significant increase in costs compared to Anger cameras read out by conventional PMTs [26].

To find a cost-effective solution to the dead edge problem, we conducted a simulation study [26], in which we investigated several gamma detector designs based on a continuous NaI(Tl) scintillator with absorptive painted edges (so-called black edges), read out by square PMTs placed in different geometries, all using a maximum likelihood (ML) algorithm for position estimation [27]. Parameters in this simulation study were chosen with a multipinhole molecular breast tomosynthesis scanner (MP-MBT) in mind which we are currently constructing. In this MP-MBT one edge of the gamma camera (referred to as the critical edge throughout this paper) has to be placed close to the patient's chest wall [26], [28], [29] and large dead edges as common in Anger cameras are not acceptable at that edge. A spatial resolution similar to that of Anger cameras is sufficient in

Manuscript received April 9, 2019; accepted May 9, 2019. Date of publication May 13, 2019; date of current version January 1, 2020. This work was supported by the Dutch Organization for Scientific Research (NWO) under VIDI Grant 12371 (Focused Imaging of Tumors). *(Corresponding author: Beien Wang.)*

B. Wang, R. Kreuger, J. Huizenga, and M. C. Goorden are with the Section of Biomedical Imaging, Department of Radiation Science and Technology, Faculty of Applied Sciences, Delft University of Technology, 2629 JB Delft, The Netherlands (e-mail: b.wang-1@tudelft.nl).

F. J. Beekman is with the Section of Biomedical Imaging, Department of Radiation Science and Technology, Faculty of Applied Sciences, Delft University of Technology, 2629 JB Delft, The Netherlands, and also with MILabs B.V., 3584 CX Utrecht, The Netherlands.

This paper has supplementary downloadable multimedia material available at http://ieeexplore.ieee.org provided by the authors.

Color versions of one or more of the figures in this paper are available online at http://ieeexplore.ieee.org.

Digital Object Identifier 10.1109/TRPMS.2019.2916386

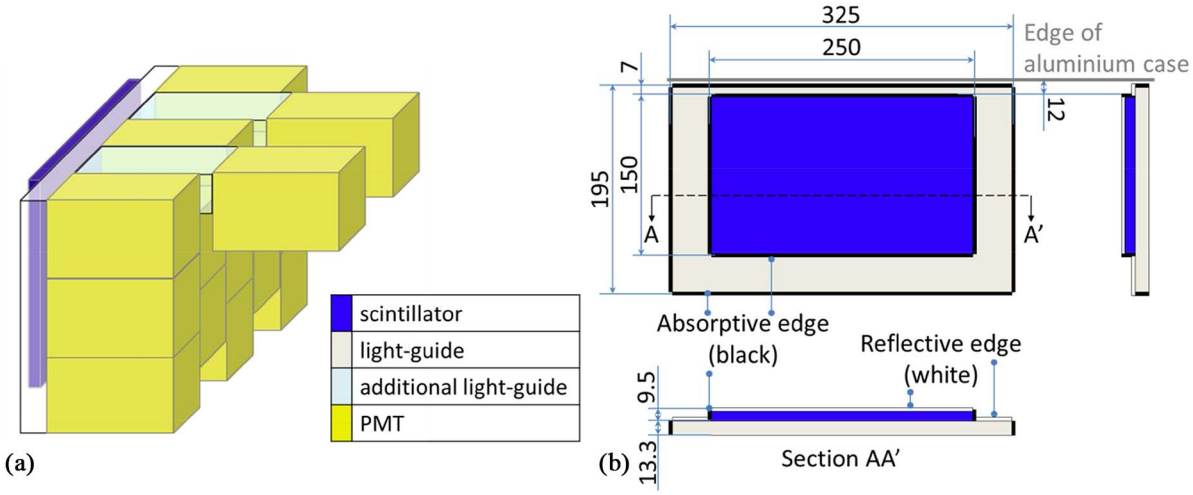

Fig. 1. (a) 3-D conceptual drawing of the studied detector geometry. (b) Schematic of the scintillator's and the light-guide's dimensions and their edge treatments.

our application as we employ pinhole magnification. From the simulation study, we found that with PMTs placed in a staggered arrangement, facilitated by an additional light-guide [Fig. 1(a)], a satisfactory positioning accuracy over the detector surface could be obtained (average horizontal and vertical spatial resolution 3.67 and 3.85 mm, respectively) while resolution loss near the edge was diminished (average horizontal and vertical spatial resolution in region 30 mm from the critical edge: 3.82 and 4.14 mm). In this paper, we present an experimental validation of this design using a prototype that has been constructed in our laboratory.

II. Methods

A. Gamma Detector Design

The gamma detector comprises a 250 × 150 × 9.5 mm^3 NaI(Tl) scintillator (Scionix B.V.) attached to a 325 × 195 × 13.3 mm^3 glass light-guide [Fig. 1(b)], and is read out by 15 Hamamatsu R6236 PMTs, each having a 54 × 54 mm^2 square sensitive area [30]. The entrance surface of the scintillator is painted with a reflective coating while the edges are absorptive [Figs. 1(b) and 2(d)]. The scintillator and light-guide are sealed in an aluminium case [the matt face in Fig. 2(a)] with a distance of about 12 mm from the upper edge of the scintillator to the upper edge of the aluminium case [see Fig. 2(b)], which is the minimum distance the manufacturer can safely achieve to preserve the hygroscopic NaI(Tl) crystal from humidity. The PMTs are attached to the light-guide in a staggered arrangement [Fig. 1(a)] and extend partly over the scintillator's left, right, and lower edges [26]. At the upper critical edge, three PMTs are directly attached to the light-guide and two other PMTs are attached via two 150-mm long additional light-guides with 60 × 31 mm^2 cross section. The additional light-guides are fused quartz bricks, polished on all six surfaces, and wrapped with white PTFE tapes. This special light-guide-PMT geometry aims to imitate partly overextending PMTs at the critical edge (where there is no physical space for truly overextending PMTs), like at the other three edges. All of the PMTs and additional light-guides are fixed in the detector

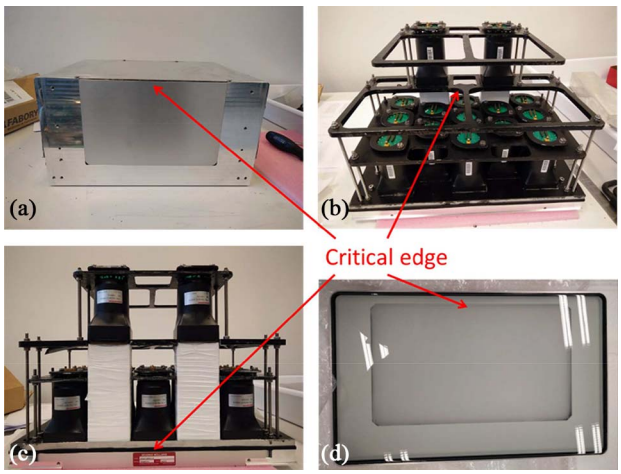

Fig. 2. Pictures of the gamma detector in various degrees of disassembly to illustrate the components inside. The position of the critical edge in each picture is marked by the red arrows. (a) Front face of the detector showing scintillator and detector box. Note that this side is facing down in (b)–(d). (b) Bottom view of the detector showing the placement of the PMTs. (c) Top view of the detector showing the additional light-guides (white blocks) and the two PMTs that are not directly placed on the light-guide attached to the scintillator, but coupled to it via the additional light-guides in a stacked structure. (d) Scintillator underneath the light-guide.

box with aluminium frames and pushed tightly against the readout window of the light-guide [Fig. 2(c)]. Optical grease (Scionix BC90/147) is applied at the interfaces to ensure good optical coupling. A light-tight box, which is painted black inside to reduce the influence of possible light leaks to PMTs, is used to hold the detector. The high voltage applied to the PMTs is 800 V.

B. Read-Out Scheme

Fig. 3 illustrates the read-out scheme. The signal from each PMT is continuously sampled through a pulse shaping circuit, which includes low pass filters and pole-zero correction by one of the ADC channels on a NI-5752 ADC board (sampling frequency 50 MHz) mounted on a NI PXIe-7961 field-programmable gate array (FPGA). The FPGA is

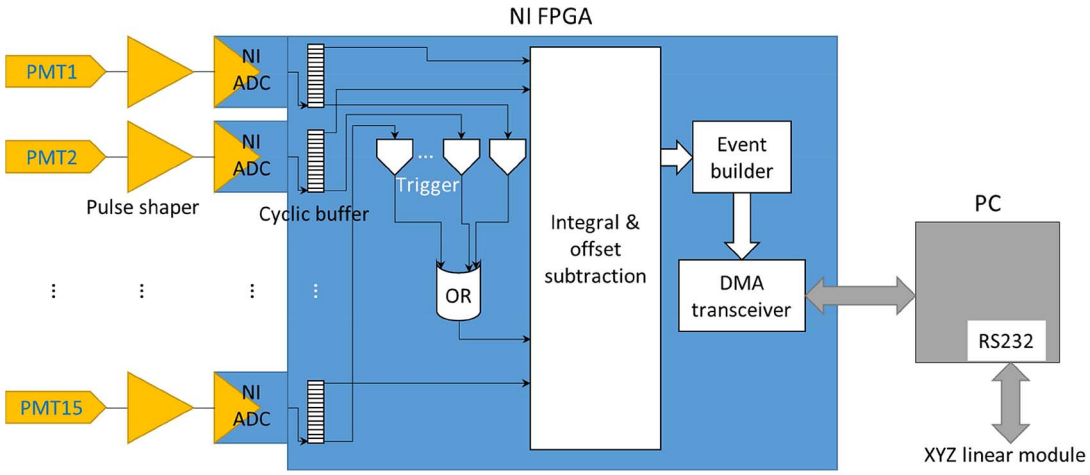

Fig. 3. PMT signal acquisition and XYZ linear module controlled by the PC.

programmed in LabVIEW and stores the 15 PMTs' ADC values in cyclic buffers with 1 k depth (20 μs). The ADC sample stream from each channel is high-pass filtered to create a trigger signal, and if any of the 15 trigger signals is above a preset threshold (logic OR operation), an event will be triggered. After a trigger, the 15 PMTs' cyclic buffers are read, and the sum of 90 samples following the trigger signal is considered to represent the PMT pulse integral, while 15 samples preceding the trigger signal are used as a baseline reference. The sum of the 90 samples subtracted by the baseline offset determined by the 15 samples is calculated. During the event processing, new triggers are not accepted. An event data structure contains the 15 integrals of PMT pulses corrected for their own individual baselines, a timestamp, an event number, and a trigger map (indicating which PMT triggered the event). The events built on FPGA are transferred to a PC through a DMA transceiver. On the PC, a LabVIEW program controls the data acquisition process.

C. Position and Energy Estimation

The interaction position and energy for each event are both estimated with Anger logic (centroid of gravity) and ML: the result of the former is the start location of the search in the latter. To improve Anger estimation, a threshold is applied to each PMT output followed by a linearity correction [31].

The ML algorithm is implemented based on a Gaussian model instead of a Poisson model, as the absolute number of optical photons collected by PMTs is hard to measure [9], [27]. If the Gaussian mean and standard deviation of the output of PMT m [$\mu_m(x, y, E)$ and $\sigma_m(x, y, E)$, referred to as reference PMT outputs] are known for gamma photons at all possible interaction location and energy combinations (x, y, E), one can calculate the likelihood that an interaction resulted in the measured PMT outputs. The interaction location and energy combination $(\hat{x}, \hat{y}, \hat{E})$ estimated by the ML algorithm is the one that maximizes this likelihood. Details of ML estimation can be found in [9], [26], [27], and [32].

The detector was calibrated only with a 140-keV beam source (see Section II-D) and the reference PMT outputs for other energies were obtained by scaling the 140-keV outputs (both μ_m and σ_m). The values of σ_m are scaled taking into account the detector intrinsic energy resolution of $\sim$5% [33], [34].

A combined estimation of the interaction location and energy $(\hat{x}, \hat{y}, \hat{E})$, i.e., a full search in 3-D space, is computationally expensive. However, for single-isotope imaging the interaction energy is only used to reject scattered events. As this can also be done by likelihood thresholding [4], [27], we also implemented an ML estimation of only the interaction position (x, y) and then applied the likelihood threshold to reject scatter.

The energy estimation in our Anger logic implementation is done by comparing the light collection of the test event with the reference mean light collection at the Anger estimated position, normalized by 140 keV (using the same reference PMT outputs from ML calibration). As a check, we also estimated the interaction energy with the same Anger approach in case we used likelihood thresholding for scatter rejection.

D. Calibration

Before assembling the 15 PMTs into the gamma camera, their relative gains were first calibrated by measuring their photopeak positions in the gamma ray detection spectra. This relative gain is used in Anger logic position estimation, which serves as a starting point of ML estimation. To this end, a small piece of NaI crystal was mounted on top of each of the PMTs, and two gamma sources, ^{57}Co and ^{241}Am, were placed near the setup. Subsequently, the relative gain of each PMT was measured for at least 48 h, and the average value after it settled to a stable value was taken. Two additional gain measurements were done to determine the attenuation of the scintillation light within the two pieces of additional light-guides. After inserting each of the two additional light-guides between the small NaI crystal and a PMT, we compared the measured photopeak position to the measurement without the light-guide and in this way we obtained the attenuation of light in the 150-mm long quartz glass. This attenuation was later accounted for in the PMT gains for the two PMTs behind the two additional light-guides. The PMT gains were used in gain corrections in all subsequent measurements.

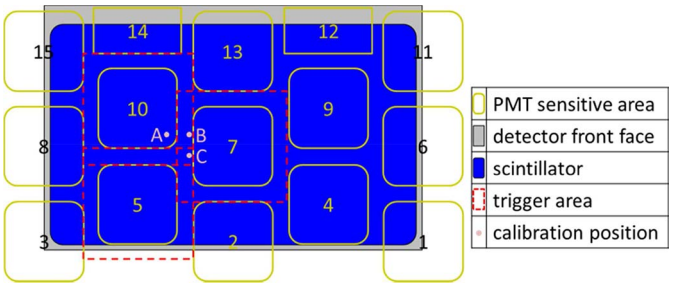

Fig. 4. Example of the criterion of setting trigger thresholds: interactions at position A (above the sensitive area of PMT 10), should trigger PMT 10 but should not trigger other PMTs; interactions at position B (above the gap between PMTs 10 and 7), should either trigger PMT 10 or 7 but should not trigger other PMTs; and interactions at position C (above the interstitial of PMTs 10, 7, and 5), should trigger PMTs 10, 7, or 5, but should not trigger other PMTs. Based on these criteria, the trigger area for every PMT can be drawn (dotted red line).

After the gain calibration, all PMTs and additional light-guides were mounted onto the gamma detector. Subsequently a trigger calibration and a position calibration were applied. To this end, a beam collimator was used as is conventional in gamma detector calibration with monolithic scintillators [4], [9], [14], [15], [27], [35], [36]. A disk with 50 MBq ^{99m}Tc inside was put in a lead-made beam collimator with a Ø1.1 $\times$ 25 mm^3 hole to obtain a perpendicular gamma photon beam on the detector. We obtained about 1000 counts per second within the photopeak with this activity. The beam collimator was fixed on an XYZ linear module with 0.03-mm positioning accuracy that could scan over the whole scintillator area.

The trigger thresholds of the PMTs were set according to the criterion that only the interactions close to a PMT could possibly trigger this PMT. Details of the criterion are illustrated with the example in Fig. 4. With the chosen thresholds, the trigger rate from the same beam should be more or less constant irrespective of placement with respect to the PMTs.

After proper PMT trigger thresholds were set, the scintillator was scanned by the collimated 140-keV photon beams in a 5-mm pitch grid (4 s per position), while recording the PMT outputs at each of these positions. The first and last rows/columns of the scanned positions were 1 mm from the nearest scintillator edges. This measurement was done to get the reference PMT outputs used in ML estimation and Anger linearity correction (see Section II-C).

Subsequently, scattered photons were removed from the calibration measurement with the following procedure consisting of three steps.

Step 1: Filter out the events that were triggered by the PMT(s) whose trigger area (see Fig. 4) did not include the known calibration position.

Step 2: Filter out the events that are outside the photopeak in the spectrum of the (sum of) *triggered* PMT output(s) [outside the photopeak is defined as being outside twice its full-width-at-half-maximum (FWHM)].

Step 3: Filter out the events that are outside the photopeak in the spectrum of the sum of *all* PMT outputs. Fig. 5 illustrates the effects of these three steps on the events measured at position B in Fig. 4.

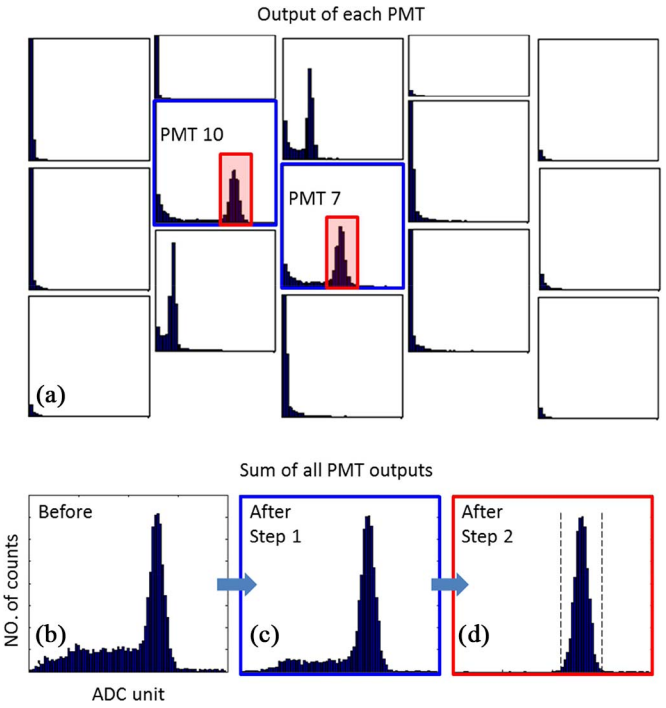

Fig. 5. Example of the effect of the three cleaning steps on the spectrum of the sum of all PMT outputs. (a) Output spectra resulting from a calibration beam at position B in Fig. 4 (same layout as the PMT layout). (b)–(d) Sum of spectra of all PMTs at each step. (b) Before the cleaning procedure. (c) After selecting the events triggered by PMTs 10 and 7. (d) After filtering out the events outside the photopeak of the sum spectrum of PMTs 10 and 7. A photopeak window is applied to (d) subsequently as step 3 to further remove residual scattered events.

After the three-step "cleaning" procedure, the μ_m and σ_m of each PMT signal over all "clean" events were calculated for a given beam position, and this 5-mm interval calibration dataset of PMTs' was then bi-cubically interpolated into a 1-mm grid to be used in ML estimation. The clean calibration data is also used to calculate the mean light collection map and light collection resolution map of the detector. Light collection is determined by summing the mean output of all PMTs, while light collection resolution is calculated by taking the FWHM of the photopeak of the spectrum of the sum of all PMT outputs and dividing it by its mean. We use the term light collection to differentiate the direct sum signal (in ADC units) from the estimated energy (in keV units). Similarly, light collection resolution is obtained from the light collection spectrum, while energy resolution is obtained from the spectrum of estimated energies.

The likelihood threshold map described in Section II-C is also generated from the calibration data. From earlier Monte Carlo simulations and [26], [27], we chose the threshold to be 15% meaning that the threshold would reject the 15% least likely events in the clean dataset. Later, we also tested other thresholds for comparison. An example likelihood spectrum with the chosen threshold is shown in Fig. 6.

E. Test Data Measurement

Several test datasets were acquired to characterize the detector's intrinsic spatial resolution, its spatial linearity, its energy

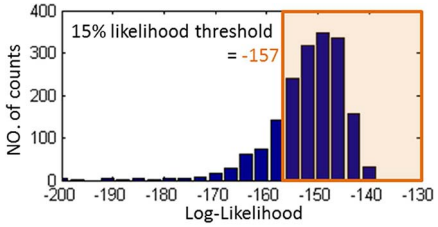

Fig. 6. Likelihood spectrum of the clean events at position B in Fig. 4. The 15% likelihood threshold at this position occurs for a log-likelihood of −157.

resolution, and its uniformity. It is important to note that the cleaning procedure in Section II-D was not applied to test data as *a priori* knowledge when evaluating the camera performance as with the test data we want to mimic the realistic situation in which the origin of the gamma photon is unknown.

The first measurement was a line spread function (LSF) measurement. According to NEMA standard [37], the intrinsic spatial resolution and linearity are to be evaluated as the profiles of LSFs, measured by masking the detector with a lead plate with vertical/horizontal slots of 1-mm width and a gamma source put far away in front of the detector. We used our beam collimator and the XYZ linear module to imitate such a measurement by sweeping the source in vertical and horizontal lines along the detector face with a speed of 7.5 mm/s back-and-forth. The count density of the lines on the detector was about 1500 counts/mm. The LSFs were put at a 10-mm interval at the center of the detector and at a 6-mm interval near the edges. We took multiple 1-mm wide profiles perpendicular to every LSF and fit a Gaussian function to every profile (default "trust-region" fit implemented in MATLAB). From this fit, we calculated the FWHM resolution and differential linearity (averaged standard deviation of the fitted profile centers of each line). The first and last lines were 3 mm from the nearest scintillator edges. The sweeping method should give equivalent result as the NEMA method, but is easier to apply (we are not in the possession of slit masks) and more flexible (different slit intervals can be tested).

The second test dataset came from a point spread function (PSF) measurement which was acquired in the same way as the calibration dataset, except that a 10-mm pitch grid in the center of the detector and a 6-mm pitch near the edges was used. The first and last rows/columns of the PSF tested positions were also 3 mm from the nearest scintillator edge. This dataset was used to characterize the energy resolution of the detector that can be obtained by different estimation algorithms. The PSFs are easy to clean compared with LSFs, as was described in the cleaning procedure in Section II-D, and for this reason they were also used to analyze in-depth the estimated PSFs from different algorithms, the scatter rejection capability with different methods, and the influence of different thresholds in likelihood threshold ML.

The third measurement done was a uniformity measurement which was performed, according to [37], by putting an uncollimated source of 13 MBq ^{99m}Tc in front of the detector 2 m away and measuring for 50 min. Then the counts were resampled in 5×5 mm^2 superpixels and filtered by a nine-point kernel ([1, 2, 1], [2, 4, 2,], [1, 2, 1]). The integral and differential uniformity were subsequently calculated over the whole detector using the definition

$$\text{uniformity} = \frac{\max - \min}{\max + \min} \times 100\% \tag{1}$$

where max and min are the maximum and minimum superpixel values on the whole detector for integral uniformity, and the local maxima and minima over five consecutive superpixels for differential uniformity. A separate uniform irradiation measurement (7 MBq ^{99m}Tc for 100 min, 2 m from detector) was done to obtain the correction map for calculating a corrected uniformity (uncorrected flood image pixel-wise divided by the correction map).

III. Results

A. Maps From Calibration Data

From the calibration data, we obtained the light collection, light collection resolution and 15% likelihood threshold maps over the detector surface (see Fig. 7). As explained in Section II-D, these three maps are subsequently used in energy estimation and scatter rejection. As the scintillator has black edges, it can be expected that the light collection is not uniform over the whole surface. This was indeed the case; compared to the central part of the detector, the edges had about 60% light collection while the corners collect about 40% as much light. The horizontal asymmetry of Fig. 7(a) may be caused by the reflector above the scintillator at the top-left corner not being properly attached to the scintillator. Consequently, the FWHM light collection resolution map was comparable to that of a conventional large area white edge Anger camera in the center (∼9%), yet poorer at the edges and corners (∼15%). Here the light collection resolution is equivalent to the optimal energy resolution of the detector as it is from a clean dataset and free from possible inaccuracy from position/energy estimation methods.

B. Position Estimation

For the measured vertical and horizontal LSFs, we used two methods to estimate the interaction position and to reject scatter events. The first method was to use ML to co-estimate both interaction position and energy (called energy ML). In this case the energy window was set to a width of twice the FWHM of the light collection resolution [Fig. 7(b)]. The LSFs estimated with this method are shown in Fig. 8(a), from which interpolated spatial resolution maps [Fig. 8(b)] are calculated. The second method used was the application of a likelihood threshold to remove scatter events (called 15% likelihood ML). The likelihood threshold is location-dependent and was shown in Fig. 7(c). The LSFs estimated with this method are provided in Fig. 8(c), from which the spatial resolution maps of Fig. 8(d) are calculated. Note that the LSFs near the edges in Fig. 8(a) and (c) were differently spaced (6-mm intervals) than in the center (10-mm intervals). It is clear that likelihood thresholding gives better results than energy ML near the edges

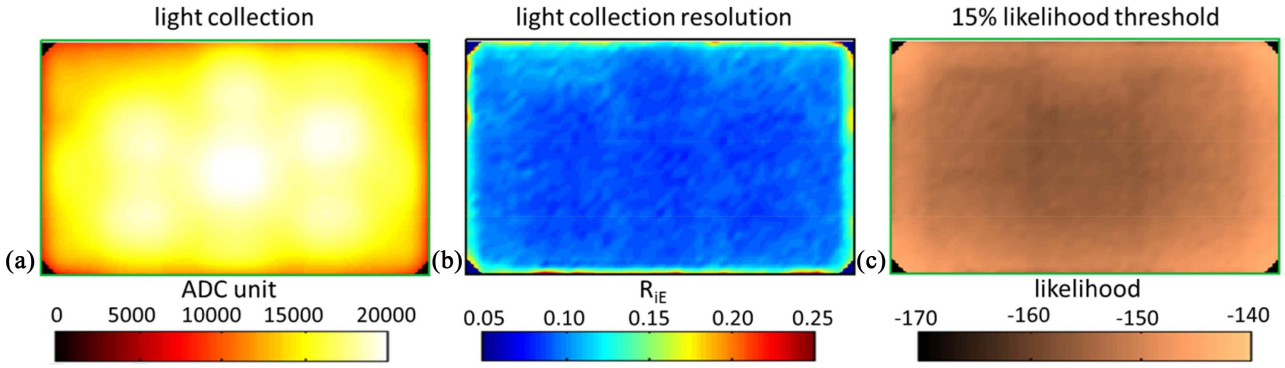

Fig. 7. From the calibration data, we acquired the (a) light collection map, (b) light collection resolution map, which is equivalent to the optimal energy resolution, and (c) likelihood threshold map (here we show the 15% likelihood threshold).

in terms of average differential linearity ($\bar{\ell}_{\text{diff}}$) and average spatial resolution ($\bar{R}_i$). For the last 30 mm from the scintillator critical edge, the energy ML method gave an average spatial resolution of 3.58 and 5.32 mm in horizontal and vertical directions, respectively, while the likelihood thresholding method gave 3.60- and 4.33-mm resolution.

C. Scatter Rejection

Intrinsic spatial resolution characterizes the FWHM of the line profiles but does not tell how well scattered events are removed (which would add background counts to the detector). Additionally, it is important to check that the algorithms do not throw away true (i.e., nonscattered) events as this would negatively impact the detector's sensitivity. Therefore, to better characterize these properties for the energy ML and 15% likelihood ML methods, we here checked these issues using the PSF measurement and compared results with that of conventional Anger logic, as this is the standard method and should still work well in the center of our detector. For this comparison, the energy window in Anger estimation was set to the same values as the energy window used in energy ML. In Fig. 9(a)–(c), all estimated test PSFs are shown for energy ML, 15% likelihood ML and Anger logic. The PSF within the yellow box (which is 25 mm from the critical edge of the scintillator) was subsequently projected onto the horizontal axis and shown in Fig. 9(d)–(f) in semilog scale for the same algorithms. These plots show that background counts were present although these were not visible on the scale of Fig. 9(a)–(c) and did not contribute to the FWHM spatial resolution. However, such background counts may play a role when reconstructing images from the projections and an algorithm which is better able to reject them is generally preferable. In this experiment, these background counts most likely originated from background radiation and scatter in the beam collimator plus its holder.

As is already clear from visual inspection of Fig. 9(d)–(f), 15% likelihood ML [Fig. 9(e)] resulted in more counts in the background than the other two methods. A quantitative comparison of the three methods' average central PSF and background count ratios is shown in Table I. Here the central PSF and background count ratios are defined as the number of counts inside or outside Ø10 mm of the irradiation position, divided by all incoming photons. As a reference, we also show these numbers for the same dataset but with scatter removed by the cleaning procedure of Section II-D and with position estimated with the ML algorithm without any event rejection (called clean data ML).

TABLE I
AVERAGE CENTRAL PSF AND BACKGROUND COUNT RATIO OF TEST POSITIONS IN THE CENTER OF THE DETECTOR OR OVER THE WHOLE DETECTOR FOR DIFFERENT ALGORITHMS

method and region		central PSF count ratio	background count ratio
centre of detector			
'clean' data ML		0.36	0.011
Anger		0.36	0.077
energy ML		0.36	0.093
ML likelihood threshold	15%	0.34	0.16
whole detector			
'clean' data ML		0.35	0.024
Anger		N/A	N/A
energy ML		0.30	0.11
ML likelihood threshold	12%	0.34	0.19
	15%	*0.34*	*0.18*
	18%	0.33	0.18
	21%	0.32	0.16
	25%	0.31	0.15
	30%	0.30	0.15
	37%	0.28	0.13
	45%	0.25	0.11

In the *centre* of the detector where Anger logic was able to obtain linear position estimation (at least 15 mm away from the left and right edges, 25 mm from the upper and lower edges), Anger logic, energy ML, and 15% likelihood ML lead to similar central PSF count ratios as the clean dataset, thus all methods have similar behavior for nonscattered events. However, the background count ratios were different: the cleaning procedure left only 1.1% background, while Anger logic and energy ML left 7.7% and 9.3%, respectively, and the 15% likelihood ML had a 16% background count ratio, which was the highest among the three methods.

Over the *whole* detector, 15% likelihood threshold still leads to similar central PSF count ratios as the clean dataset (34% versus 35%, respectively), while the difference in background count ratios between these two methods was still large (2.4% versus 18%); energy ML had a reduced central PSF count ratio

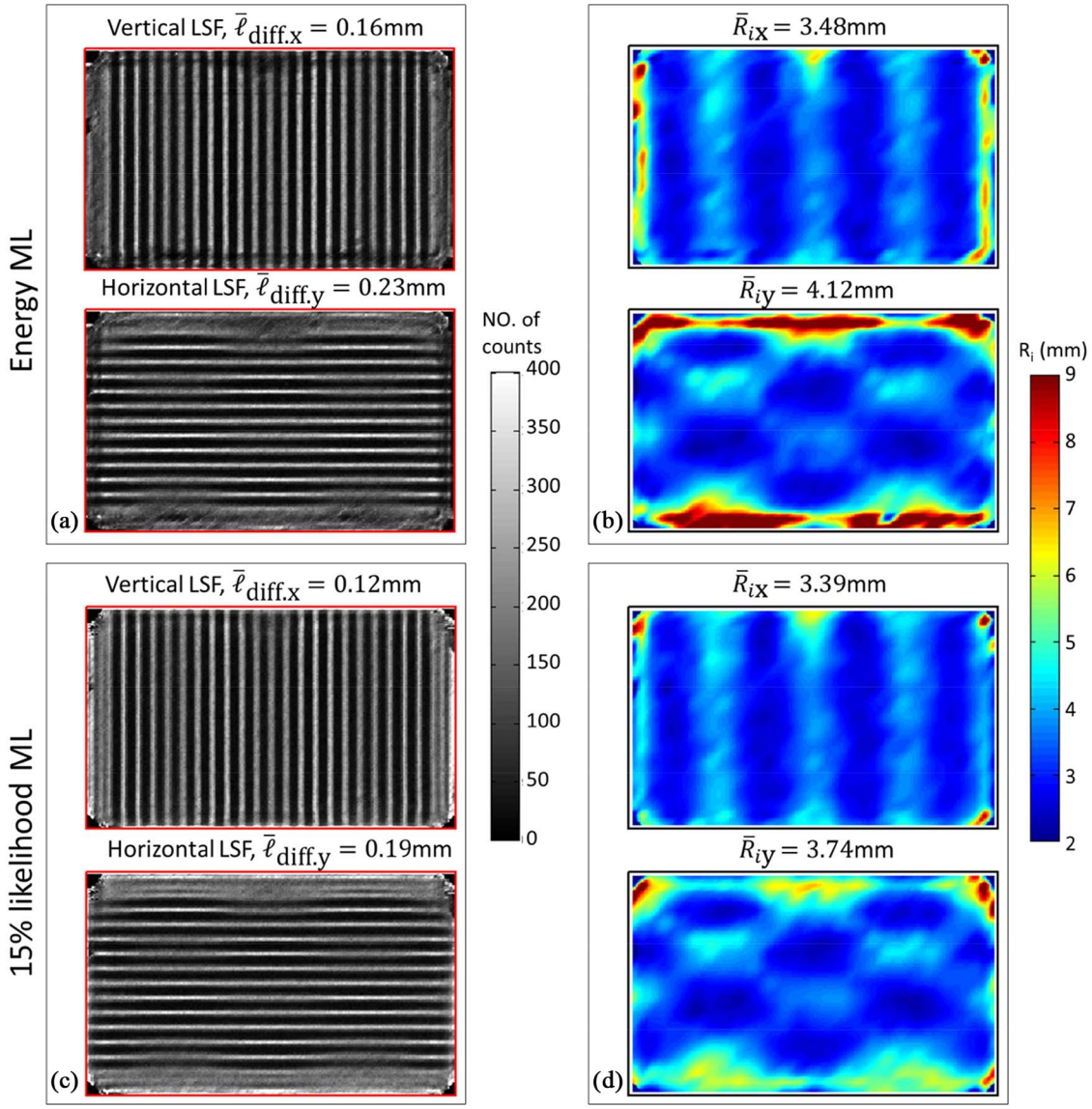

Fig. 8. LSF test dataset as measured by the gamma detector using different algorithms for position estimation. (a) Detector images obtained with an (**x**, **y**, **E**) 3-D ML search, with (b) resulting interpolated spatial resolution maps. (c) Detector images obtained with likelihood thresholding (threshold set at 15% least likely calibration data) with (d) resulting calculated and interpolated spatial resolution maps. The averaged differential linearity $\bar{\boldsymbol{\ell}}_{\mathbf{diff}}$ and intrinsic spatial resolution $\bar{\mathbf{R}}_{\boldsymbol{i}}$ are also provided. Note that the LSFs near the edges in (a) and (c) were differently spaced (6-mm intervals) than in the center (10-mm intervals).The rectangular frame in all the images marks the edge of the scintillator.

over the whole detector (30%) because the position estimation near the edges was quite poor. We also varied the likelihood threshold to see if that is a proper way to reject more background counts. However, from Table I it can be seen that using a higher threshold leads to rejection of more background only at the expense of rejecting as many valid events (events near irradiated position). To evaluate how the estimated energy from energy ML correlates to the calculated likelihood from 15% likelihood ML, we made a scatter plot for the events' likelihoods and energies which is shown in the supplementary material.

D. Energy Resolution

Fig. 9(g)–(i) showed the estimated energy resolution obtained with the three methods. At the central region, all three methods gave similar energy resolution of about 10%, which, understandably, is poorer than the light collection resolution in Fig. 7(b), as this is the best achievable energy resolution obtained from calibration data from which scatter was removed. The linear region of Anger logic is limited to the central part of the detector, so for Anger logic only the energy resolution in the central part is shown. An unreasonable feature in Fig. 9(h) is that the edges have even better energy resolution than the central part. We checked the estimated energy spectra near the edges and the 15% likelihood ML method tends to estimate a test event at the position where the reference light collection is similar to the test event's light collection. We, therefore, cannot use the energy estimation results near the edges from the 15% likelihood ML to facilitate scatter rejection.

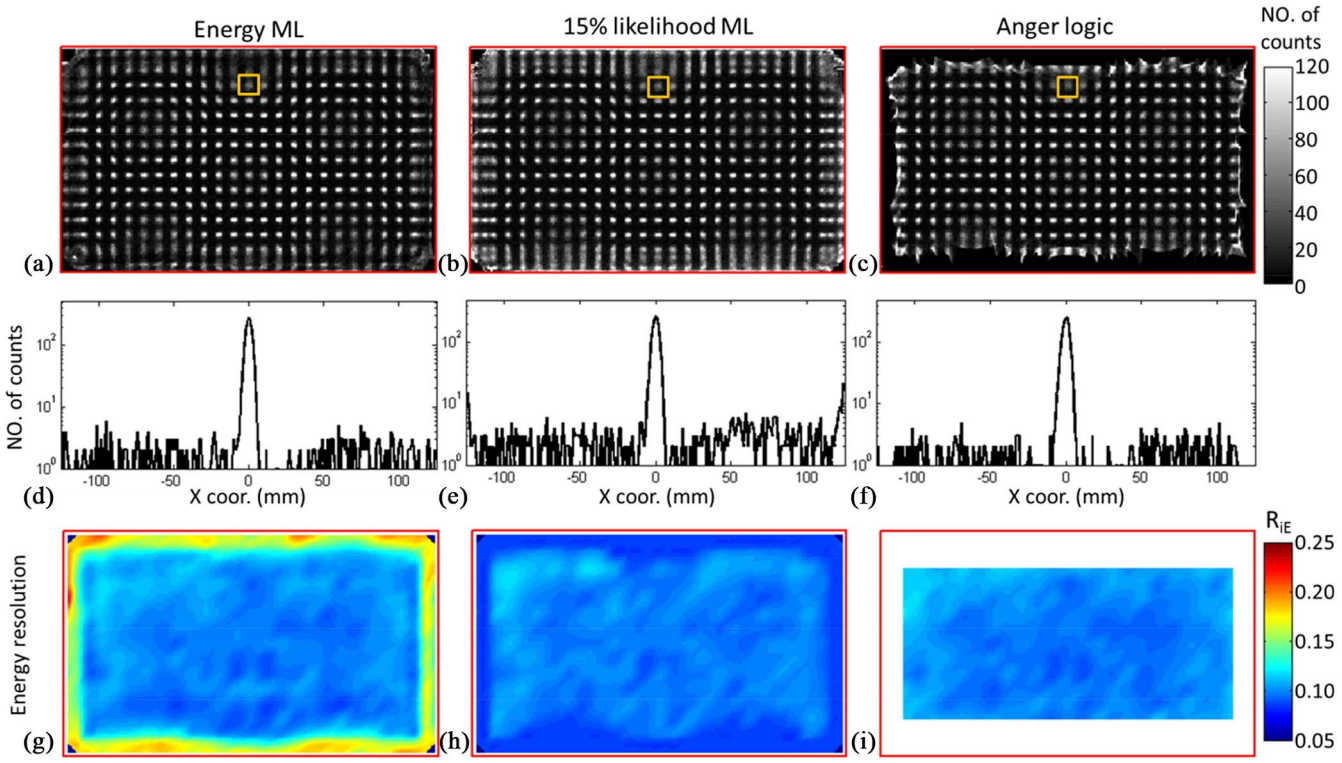

Fig. 9. (a) Test PSFs estimated with the energy ML method. (b) Test PSFs estimated with 15% likelihood ML. (c) Test PSFs estimated with Anger estimation; the central linear region is up to about 25 mm to the edges. (d)–(f) Projections of the marked PSF in the yellow boxes in (a)–(c) in semilog scale. (g)–(i) Spatial distribution of the energy resolution from (a)–(c). In (i), only the energy resolution in the central part of the detector is calculated as the position estimation is completely distorted at the edges.

E. Uniformity

As was shown in Sections III-B and III-C, energy ML did not give an equally accurate position estimation near the critical edge as 15% likelihood ML and it was also slow, therefore 15% likelihood ML is the preferred method for our MP-MBT application. For this reason, we only applied the 15% likelihood threshold algorithm to the uniformity measurement data. Fig. 10(a) shows the flood image obtained in this way. Piled-up counts can be observed at the edges and distortions occur at the corners. The source of the pile-ups are discussed in Section IV. With the approach described in Section II-E, in the central region, defined as the detector area more than 5 mm away from any edge, we calculated the integral uniformity of the detector to be 12% and the maximum differential uniformities to be 8% and 7% in horizontal and vertical direction, respectively, without any uniformity correction. After uniformity correction [shown in Fig. 10(b)], in the same region the integral uniformity was 1.7% while the maximum differential uniformities were 1.2% and 1.3% in horizontal and vertical directions.

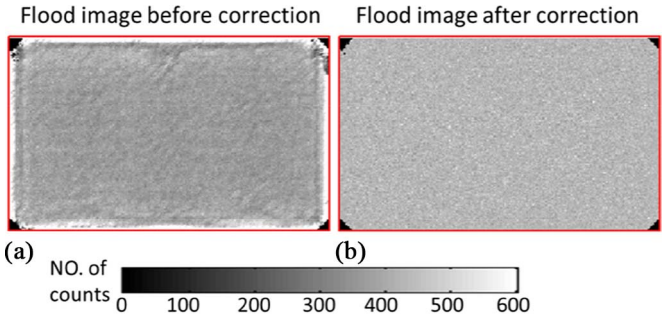

Fig. 10. Flood image measured with a 13 MBq ^{99m}Tc source placed about 2 m in front of the detector for 50 min (a) without any uniformity correction, and (b) after uniformity correction. Pixel size shown is 1 mm^2. The rectangular frame marks the edge of the scintillator.

IV. Discussion

From the measurement results shown in Fig. 8, it can be inferred that the proposed detector using ML position estimation with likelihood thresholding gives an intrinsic spatial resolution comparable to that of conventional Anger cameras in the centre (about 3.5-mm resolution). Near the critical edge, the vertical resolution is somewhat degraded (4.3 mm on average in the last 30 mm from edge), but this region is completely useless in conventional Anger cameras. Energy ML gives much poorer spatial resolution near the scintillator's edges and is slower than the 15% likelihood threshold method. Therefore, energy ML seems not to be the most suitable algorithm for this detector. The test positions are up to 3 mm to the scintillator edges while the calibration positions are up to 1 mm to the scintillator edges. Considering the good spatial linearity and uniformity near the critical edge with 15% likelihood ML, it is fair to say that the dead edges are less than 3 mm from the scintillator edge. Including the 12-mm sealing required to preserve the enclosing hygroscopic NaI(Tl) crystal, the overall dead edge of the detector is thus less than

15 mm. This is much better than the 4-cm dead edge for conventional gamma cameras, and should be sufficient to realize the proposed and simulated MP-MBT for which we already performed simulations with 15-mm dead edge gamma camera and found results very similar to those in [28] and [29]. If, in the future, the sealing material over the critical edge could be reduced while the NaI(Tl) is still well protected, the scintillator could be positioned closer to the critical edge and the overall critical edge could be even reduced.

Ideally, to evaluate the effect of the two additional light guides one would like to experimentally compare different gamma camera geometries. Unfortunately, this is not possible due to practical constraints (rearranging the PMTs in the current detector may lead to damage). However, in an earlier study we have simulated a gamma detector of similar dimension as the assembled one but with different PMT arrangements [26], including the current one and an arrangement without additional light-guides. The experimental detector compares well to the simulation results in terms of spatial resolution. Especially, the similarity in how resolution varies over the detector area is striking; the best resolution is obtained in the interstitials between PMTs, a poorer resolution is achieved above the centers of PMTs, and the poorest resolution is above the centre of the edge PMTs. Based on these similarities with simulations, we believe that for a detector without additional light guides the last 30-mm critical edge would have spatial resolution similar to that above PMT 13 (see Fig. 4) in the assembled detector which is among the poorest areas of the detector. This would seriously hamper our MP-MBT scanner's performance.

Additionally, we would like to point out that a design with additional light guides along the full critical edge was also simulated [26]. While such a design is beneficial for resolution near the critical edge, the downside is a much poorer spatial resolution along the opposite edge. Therefore, we chose to build the current staggered design. Some simulation results are presented in the supplementary material for better insight.

From Table I, the 15% likelihood threshold seems to be a proper choice as the number of accepted counts in the PSF is comparable to that of Anger logic, indicating that valid events are accepted. The background found in the test data [as shown in Fig. 9(e)] is hard to get rid of by adjusting the likelihood threshold, as is evident from the numbers in Table I. This background also exists for energy ML and Anger position estimation [Fig. 9(d) and (f)], but its magnitude is about 40% smaller for these methods than for 15% likelihood ML. Similarly, we checked that in the LSF measurements, the background counts (counts within 5 mm from the scanned lines) also have about 40% smaller magnitude for energy ML than for 15% likelihood ML (in the centre of the detector). This means that energy windowing is still better at scatter rejection than likelihood thresholding, and this could be a reason to use energy windowing in the central region of the detector and use likelihood thresholding only near the edges. Whether this background will be a big issue or not has to be checked in a real scanner where scattered photons from the torso are present and need to be rejected.

The flood image in Fig. 10(a) contains quite obvious pile-up counts at the edges. These pile-ups are partly due to the ML algorithm, which tends to give a certain amount of pile-ups at the end of its search grid. In Figs. 8(e) and (g) and 9(b), there are indeed some observable pile-ups in the last pixels near the edges of the scintillator, though the effect is very small. The main source of the pile-ups is probably the presence of the aluminium case of the scintillator. As was mentioned in Section II-A, the scintillator is placed in an aluminium case with a thickness of 12 mm at the critical edge and 4 mm to other edges. The critical edge requires more sealing space as the light-guide does not extend over the scintillator's edge very much, while at the other three edges, the light-guide edges extend about 30 mm over the scintillator's edge. As the cross section for scatter of 140-keV gamma photons in aluminium is large, extra scatter events will take place near the critical edge. It should be kept in mind that when using the camera, the aluminium sides of the detector should be shielded.

In SPECT imaging, scatter rejection with simply one photopeak window is not always sufficient. A triple energy window scatter correction is often applied [38], [39]. With the ML likelihood thresholding method, the counts in the side energy windows are mostly rejected and thus we can no longer implement a triple energy window correction. One may think of using three reference PMT output sets plus three likelihood threshold sets for three energy windows (photopeak and two side energies) respectively, in order to obtain projection images of the three energy windows, and then apply a triple energy window scatter correction. The reference PMT outputs for the 140-keV photopeak are directly calculated from the calibration measurement, and to get the reference PMT outputs in the two side energy windows, we may scale the calibration measurement to the side window energies, and then follow the process in Section II-D. This idea will be tested in the future with phantom scans.

The current detector is designed and build to be applied in a MP-MBT system in which there is one critical edge. However, the proposed additional light-guide design can in principle be extended to all edges of the detector if required, so that it can meet the requirements of dedicated cardiac SPECT scanners, or any other applications in which minimizing dead edges is important.

V. Conclusion

In conclusion, we have presented and experimentally evaluated a black-edge gamma detector with staggered PMT arrangement in combination with ML position estimation. We found that the detector has the ability to also estimate events near the scintillator's edges; the detector dead edge including the 12-mm sealing case is less than 15 mm. The detector, therefore, is a good and cost-effective solution when conventional cameras with roughly 4-cm dead edges are not acceptable.

VI. Acknowledgment

The authors would like to thank M. Verleg and E. van der Wal for their help of making the detector box into reality.

REFERENCES

[1] H. O. Anger, "Scintillation camera," *Rev. Sci. Instrum.*, vol. 29, no. 1, pp. 27–33, 1958.

[2] R. Freifelder, A. T. Haigh, and J. S. Karp, "Reducing edge effects and improving position resolution in position-sensitive NaI(Tl) detectors," *IEEE Trans. Nucl. Sci.*, vol. 40, no. 2, pp. 208–213, Apr. 1993.

[3] P. Vaska, M. J. Petrillo, and G. Muehllehner, "Virtual PMTs: Improving centroid positioning performance near the edges of a gamma camera detector," *IEEE Trans. Nucl. Sci.*, vol. 48, no. 3, pp. 645–649, Jun. 2001.

[4] T. D. Milster *et al.*, "A full-field modular gamma camera," *J. Nucl. Med.*, vol. 31, no. 5, pp. 632–639, May 1990.

[5] M. Bocher *et al.*, "A fast cardiac gamma camera with dynamic SPECT capabilities: Design, system validation and future potential," *Eur. J. Nucl. Med. Mol. Imag.*, vol. 37, no. 10, pp. 1887–1902, Oct. 2010.

[6] M. Rozler, H. N. Liang, H. Sabet, and W. Chang, "Development of a cost-effective modular pixelated NaI(Tl) detector for clinical SPECT applications," *IEEE Trans. Nucl. Sci.*, vol. 59, no. 5, pp. 1831–1840, Oct. 2012.

[7] D. R. Gilland, B. L. Welch, L. Lee, B. Kross, and A. G. Weisenberger, "Evaluation of a novel collimator for molecular breast tomosynthesis," *Med. Phys.*, vol. 44, no. 11, pp. 5740–5748, Nov. 2017.

[8] C. B. Hruska, A. L. Weinmann, and M. K. O'Connor, "Proof of concept for low-dose molecular breast imaging with a dual-head CZT gamma camera. Part I. Evaluation in phantoms," *Med. Phys.*, vol. 39, no. 6, pp. 3466–3475, Jun. 2012.

[9] J. Joung, R. S. Miyaoka, and T. K. Lewellen, "cMiCE: A high resolution animal PET using continuous LSO with a statistics based positioning scheme," *Nucl. Instrum. Meth. A Accelerators Spectrometers Detectors Assoc. Equip.*, vol. 489, nos. 1–3, pp. 584–598, Aug. 2002.

[10] A. K. Krizsan *et al.*, "A promising future: Comparable imaging capability of MRI-compatible silicon photomultiplier and conventional photosensor preclinical PET systems," *J. Nucl. Med.*, vol. 56, no. 12, pp. 1948–1953, Dec. 2015.

[11] S. Majewski *et al.*, "Optimization of a mini-gamma camera based on a 2×2 array of Hamamatsu H8500 PSPMTs," *Nucl. Instrum. Meth. A Accelerators Spectrometers Detectors Assoc. Equip.*, vol. 569, no. 2, pp. 215–219, Dec. 2006.

[12] T. Yanagida *et al.*, "Development of Pr:LuAG scintillator array and assembly for positron emission mammography," *IEEE Trans. Nucl. Sci.*, vol. 57, no. 3, pp. 1492–1495, Jun. 2010.

[13] M. A. N. Korevaar, J. W. Heemskerk, M. C. Goorden, and F. J. Beekman, "Multi-scale algorithm for improved scintillation detection in a CCD-based gamma camera," *Phys. Med. Biol.*, vol. 54, no. 4, pp. 831–842, Feb. 2009.

[14] K. Deprez, S. Vandenberghe, B. Vandeghinste, and R. Van Holen, "FlexiSPECT: A SPECT system consisting of a compact high-resolution scintillation detector (SPECTatress) and a lofthole collimator," *IEEE Trans. Nucl. Sci.*, vol. 60, no. 1, pp. 53–64, Feb. 2013.

[15] C. Domingo-Pardo *et al.*, "A position sensitive γ-ray scintillator detector with enhanced spatial resolution, linearity, and field of view," *IEEE Trans. Med. Imag.*, vol. 28, no. 12, pp. 2007–2014, Dec. 2009.

[16] R. S. Miyaoka *et al.*, "Resolution properties of a prototype continuous miniature crystal element (cMiCE) scanner," *IEEE Trans. Nucl. Sci.*, vol. 58, no. 5, pp. 2244–2249, Oct. 2011.

[17] W.-H. Wong, J. Uribe, K. Hicks, and G. Hu, "An analog decoding BGO block detector using circular photomultipliers," *IEEE Trans. Nucl. Sci.*, vol. 42, no. 4, pp. 1095–1101, Aug. 1995.

[18] Z. Li, M. Wedrowski, P. Bruyndonckx, and G. Vandersteen, "Nonlinear least-squares modeling of 3D interaction position in a monolithic scintillator block," *Phys. Med. Biol.*, vol. 55, no. 21, pp. 6515–6532, Nov. 2010.

[19] R. Marcinkowski *et al.*, "Sub-millimetre DOI detector based on monolithic LYSO and digital SiPM for a dedicated small-animal PET system," *Phys. Med. Biol.*, vol. 61, no. 5, pp. 2196–2212, Mar. 2016.

[20] D. R. Schaart *et al.*, "A novel, SiPM-array-based, monolithic scintillator detector for PET," *Phys. Med. Biol.*, vol. 54, no. 11, pp. 3501–3512, Jun. 2009.

[21] A. Groll *et al.*, "Hybrid pixel-waveform (HPWF) enabled CdTe detectors for small animal gamma-ray imaging applications," *IEEE Trans. Radiat. Plasma Med. Sci.*, vol. 1, no. 1, pp. 3–14, Jan. 2017.

[22] G. A. Kastis *et al.*, "Gamma-ray imaging using a CdZnTe pixel array and a high-resolution, parallel-hole collimator," *IEEE Trans. Nucl. Sci.*, vol. 47, no. 6, pp. 1923–1927, Dec. 2000.

[23] L. Verger *et al.*, "Performance and perspectives of a CdZnTe-based gamma camera for medical imaging," *IEEE Trans. Nucl. Sci.*, vol. 51, no. 6, pp. 3111–3117, Dec. 2004.

[24] D. J. Wagenaar, S. Chowdhury, J. C. Engdahl, and D. D. Burckhardt, "Planar image quality comparison between a CdZnTe prototype and a standard NaI(T1) gamma camera," *Nucl. Instrum. Methods Phys. Res. A Accelerators Spectrometers Detectors Assoc. Equip.*, vol. 505, nos. 1–2, pp. 586–589, Jun. 2003.

[25] L. Cai *et al.*, "MRC-SPECT: A sub-500 μm resolution MR-compatible SPECT system for simultaneous dual-modality study of small animals," *Nucl. Instrum. Methods Phys. Res. A Accelerators Spectrometers Detectors Assoc. Equip.*, vol. 734, pp. 147–151, Jan. 2014.

[26] B. Wang *et al.*, "Novel light-guide-PMT geometries to reduce dead edges of a scintillation camera," *Physica Medica*, vol. 48, pp. 84–90, Apr. 2018.

[27] H. H. Barrett, W. C. J. Hunter, B. W. Miller, S. K. Moore, Y. Chen, and L. R. Furenlid, "Maximum-likelihood methods for processing signals from gamma-ray detectors," *IEEE Trans. Nucl. Sci.*, vol. 56, no. 3, pp. 725–735, Jun. 2009.

[28] J. van Roosmalen, F. J. Beekman, and M. C. Goorden, "System geometry optimization for molecular breast tomosynthesis with focusing multi-pinhole collimators," *Phys. Med. Biol.*, vol. 63, no. 1, Dec. 2017, Art. no. 015018.

[29] J. van Roosmalen, M. C. Goorden, and F. J. Beekman, "Molecular breast tomosynthesis with scanning focus multi-pinhole cameras," *Phys. Med. Biol.*, vol. 61, no. 15, pp. 5508–5528, Jul. 2016.

[30] *Photomultiplier Tubes and Related Products*. Hamamatsu, Japan: Hamamatsu Photonics K.K., 2016.

[31] J. L. Villena, G. Tapias, E. Lage, R. Kreuger, and F. J. Beekman, "Evaluation of a 25–511keV list mode readout system for a large field-of-view gamma camera," in *Proc. IEEE Nucl. Sci. Symp. Med. Imag. Conf.*, 2010, pp. 2168–2173.

[32] M. Ruiz-Gonzalez, V. Bora, and L. R. Furenlid, "Maximum-likelihood estimation of scintillation pulse timing," *IEEE Trans. Radiat. Plasma Med. Sci.*, vol. 2, no. 1, pp. 1–6, Jan. 2018.

[33] P. Dorenbos, J. T. M. de Haas, and C. W. E. van Eijk, "Non-proportionality in the scintillation response and the energy resolution obtainable with scintillation crystals," *IEEE Trans. Nucl. Sci.*, vol. 42, no. 6, pp. 2190–2202, Dec. 1995.

[34] M. Moszyński, J. Zalipska, M. Balcerzyk, M. Kapusta, W. Mengesha, and J. D. Valentine, "Intrinsic energy resolution of NaI(Tl)," *Nucl. Instrum. Methods Phys. Res. A Accelerators Spectrometers Detectors Assoc. Equip.*, vol. 484, nos. 1–3, pp. 259–269, May 2002.

[35] L. R. Furenlid *et al.*, "FastSPECT II: A second-generation high-resolution dynamic SPECT imager," *IEEE Trans. Nucl. Sci.*, vol. 51, no. 3, pp. 631–635, Jun. 2004.

[36] X. Li, M. Ruiz-Gonzalez, and L. R. Furenlid, "An edge-readout, multilayer detector for positron emission tomography," *Med. Phys.*, vol. 45, no. 6, pp. 2425–2438, Jun. 2018.

[37] *NEMA Standards Publication NU 1-2007: Performance Measurement of Gamma Cameras*. Arlington, VA, USA: Nat. Elect. Manuf. Assoc., 2007.

[38] B. Wang *et al.*, "Voxelized ray-tracing simulation dedicated to multi-pinhole molecular breast tomosynthesis," *Biomed. Phys. Eng. Exp.*, vol. 3, no. 4, Aug. 2017, Art. no. 045021.

[39] K. Ogawa, Y. Harata, T. Ichihara, A. Kubo, and S. Hashimoto, "A practical method for position-dependent Compton-scatter correction in single photon-emission CT," *IEEE Trans. Med. Imag.*, vol. 10, no. 3, pp. 408–412, Sep. 1991.